

# Multiphysics Simulation of In-Service Welding and Induction Preheating: Part 1

A FEM to simulate in-service welding qualification considering induction preheating and fluid flow in a coupled solution is presented

BY K. C. RIFFEL, R. H. G. E SILVA, A. J. RAMIREZ, A. F. F. ACUNA, G. DALPIAZ, AND M. T. P. PAES

## Abstract

A finite element model was developed using a multiphysics finite element analysis (FEA) coupling heat transfer, fluid flow, and electromagnetic heating. Part 1 presents the software implementation and model equations *beside* the mesh setting and modeling approach to simulate circumferential welding of Type B sleeve repair. The simulation was divided into four steps running sequentially for each physic solved in the model. Induction preheating was simulated and validated by comparing simulated temperature with experimental measurements. The multiphysics model differs from the usual simulations present in the literature, expressing more reliability in the results and making way for more-complete modeling for in-service applications.

## Keywords

- Type B Sleeve Repair
- Welding Modeling
- Finite Element Analysis
- GMAW-P For In-Service Welding

## Introduction

In-service welding is a very important demand in the oil and gas industry. The need for it may arise for repair or installing bypasses without stopping fluid flow (Refs. 1–3). Such a welding technique aims to mitigate pipeline downtime, keeping the supply of hydrocarbon and compromising the operational capacity as little as possible. Examples of in-service welding applications include Type B sleeves, patches, weld overlay, and fittings for hot tapping (Refs. 4–7).

In most cases, in-service welding is susceptible to a higher cooling rate compared to a conventional weld. This is due to a fluid flow that may be at a high flow rate and pressure increasing heat flux on the inner wall. The faster cooling makes the welded metal and the heat-affected zone (HAZ) prone to the formation of brittle microstructures and defects, such as lack of fusion (Ref. 8). In such operations, the combination of high-hardness microstructures with a higher level of diffusible hydrogen (available on the workpiece due to hydrocarbon contaminants, condensation in temperatures below the dew point, and oxides that are hygroscopic and can retain humidity as well as in the weld consumable) makes the welded joint susceptible to hydrogen-induced cracking (HIC). Moreover, flammable fluids also create concern regarding the burn through/blowout risk (Refs. 9, 10). Such issues bring great complexity to in-service welding, showing the necessity for proper control using techniques/processes that mitigate the risk of defects and increase safety.

Therefore, parameters and variables that involve the welding process and the qualification of a procedure involve the mounting of complex systems with the circulation of water to produce a greater thermal severity (Refs. 1–3, 6, 7). Thus, the use of methods for the predictability of results, as a function of certain input parameters, is a tool that enables an understanding of physical phenomena that are difficult to measure as well as providing potentially more dynamic testing procedures, reducing time and raw material costs.

One of the most-used forms of numerical simulation concerns the finite element method (FEM). FEM simulation of in-service welding was applied in previous research by Huang et al. (Ref. 11) and Guest et al. (Ref. 12). The authors tried to predict the temperature distribution and thermal cycles of the welding process, disregarding the effect of auxiliary techniques, which are mandatory for in-service applications, such as preheating of the part. In the same way, fluid flow was not modeled by the authors. Ignoring important variables (preheating method and fluid flow) induces large errors and an underestimation of the temperature and thermal cycle prediction.

<https://doi.org/10.29391/2024.103.005>

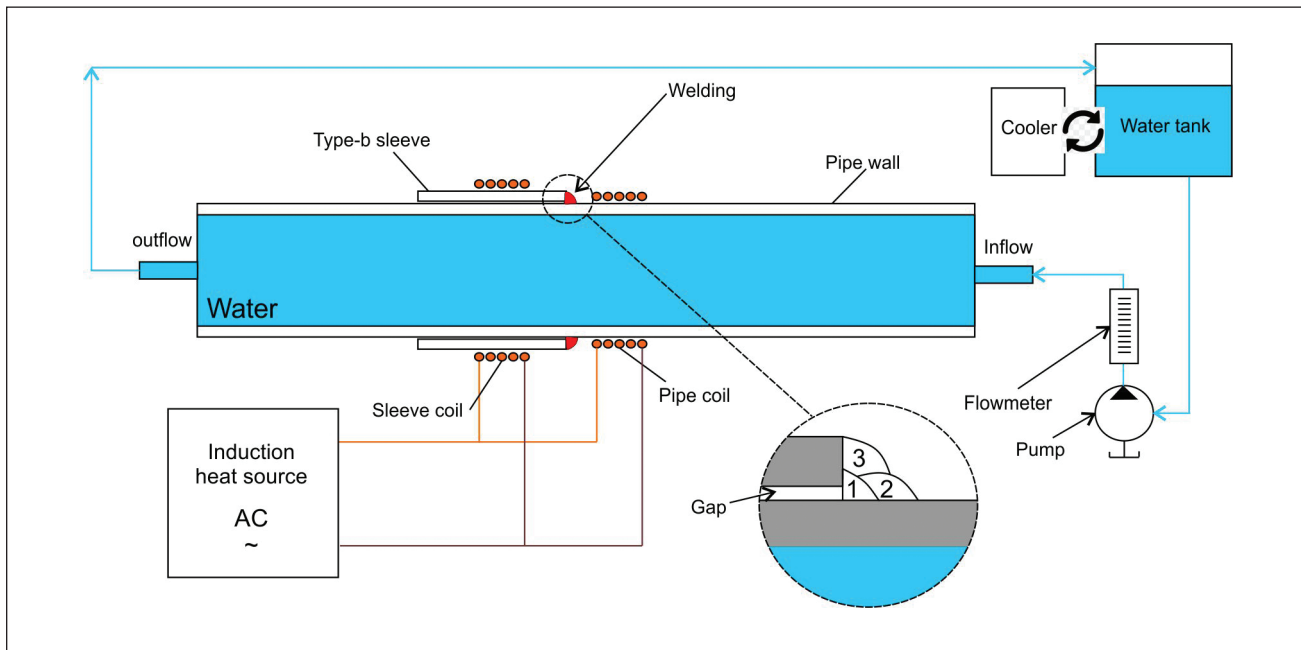


Fig. 1 – Schematic of the water looping for in-service welding qualification.

The simplification of the modeling is a result of the complex multiphysics existing in the process, making the problem not tractable if too many phenomena are considered in the problem. Compared to conventional welding simulations, in-service welding inserts a few more physical variables. Alian et al. (Ref. 13) developed a thermomechanical finite element analysis (FEA) for in-service welding, aiming to verify the influence of the welding sequence over the circumferential distortion and residual stress in the pipe. Wang et al. (Ref. 14) created a model to analyze temperature distribution and thermal cycles for in-service fillet welding of Type B sleeves. The authors proposed a comparison of the cooling rate of the weld depending on the convective flux of different fluids. Even though both papers created thermal models to analyze temperature distribution, in all cases, significant variables were simplified concerning the welding and fluid flow models. For example, the internal heat transfer coefficient ( $h$ ) was analytically calculated based on a fully developed flow, which is a completely different behavior from a reduced pipe length used in welding qualification following the standard API 1104, *Standard for Welding Pipelines and Related Facilities*, Appendix B (Ref. 6) and laboratory experiments.

Therefore, this paper aims to show the in-service welding simulation using a multiphysics approach. The research was divided into two technical papers (Part 1 and Part 2). This first manuscript discusses the steps in creating a multiphysics model focused on implementing induction preheating and fluid flow for a reduced mock-up. Using a carbon steel pipe and a Type B sleeve repair, a water loop was mounted to simulate greater heat flux and cooling rate. Moreover, the use of electromagnetic induction preheating for high cooling rate repairs is an innovative technique in which an electromagnetic field generated by an alternating current at high frequency can induce an eddy current that circulates through the component, causing heating by the Joule effect (Refs.

15, 16). Consequently, the purpose of Part 1 of this research is to present a model using FEM considering the modeling of the preheating by electromagnetic induction, the fluid flow inside the pipe, and the welding heat source. Complementary, Part 2 will present simulation results and validation of the multiphysics in-service welding model created in Part 1, comparing post-processing results with experimental data, such as welding cross-section macrographs and thermal cycles.

## Experimental Procedure

### Materials and Methods

The experimental part of this work was carried out in a water loop to emulate the in-service welding of Type B sleeves, as shown in the schematic of Fig. 1. The sample was a carbon steel API 5L Grade B pipe 2 m (6.561 ft) in length, 324 mm (12.756 in.) in diameter, and 9.5 mm (0.374 in.) thick. The water flow was kept at 380 l (100.385 gal)/min measured using a flowmeter, and the water tank was connected to a cooler, keeping the inflow temperature at 20°C (68°F), according to Fig. 1.

Experiments and simulations were carried out simultaneously in this research. Firstly, the model was set to simulate only the fluid flow coupled with the electromagnetic physics (equations are detailed in the next topic). Experimentally, the induction power source was a Miller ProHeat™ 35 with two flexible copper cables (coils) 10 mm (0.394 in.) in diameter. The power source was set to work at its maximum power of 35 kW, resulting in an AC frequency of 10.4 kHz and an RMS current of 350 A. These values were fixed for all tests and represent the boundary condition defined by the induction heating model (more details regarding the boundary conditions can be verified in Appendix 1). For the Type B sleeve

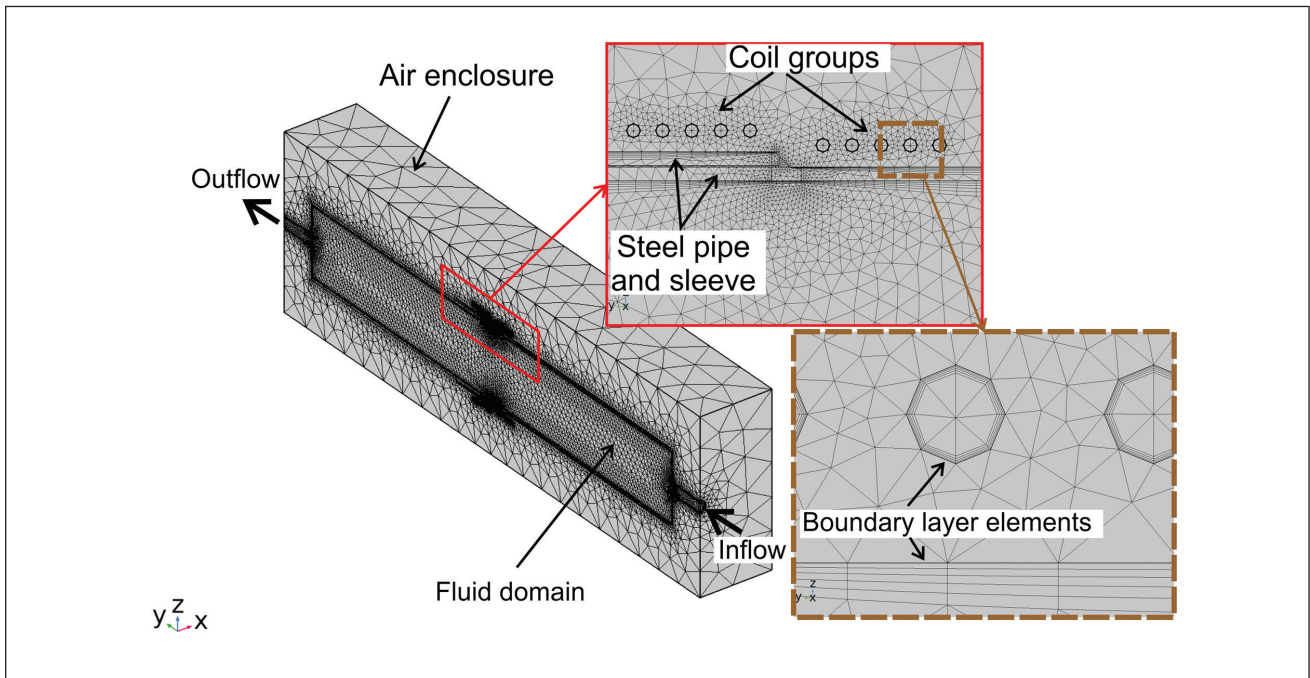


Fig. 2 – Geometry and mesh details applied to in-service welding simulation model.

welding, a double-coil configuration was set according to Fig. 1, in which one coil heated the sleeve and the other one heated the pipe simultaneously. The maximum preheating temperature was limited and controlled to 400°C (752°F) right beneath the sleeve coil.

During the tests, the temperature was measured using Type K thermocouples 1 mm (0.039 in.) in diameter. The thermal analysis and temperature acquisition were analyzed with a portable measurement system, IMC Welding SAP V471 (Ref. 17). Thermography was also carried out with a FLIR SC7200 heat camera to measure the temperature field in the induction heating simultaneously with the thermocouples, working as a calibration device to the thermographic image.

GMAW with pulsed current (GMAW-P) was applied to the girth welding with the electrical parameters presented in Table 1, which were used as boundary conditions to the modeled heat source. Three weld beads were laid sequentially, as presented in detail in Fig. 1. More details regarding the welding equipment will be presented in Part 2 of this work.

The FEM simulations were developed on COMSOL Multiphysics® 6.1 software, applying the differential equations of the AC/DC (alternate/direct current) and heat transfer modules. The computer setup was an AMD Ryzen™ 7 3800X microprocessor with eight cores and 16 threads working at a clock frequency of 3.9 GHz, 64 GB of RAM DDR4 at 2666 MHz, and an Adata solid state drive with 1 Tb of storage capability and reading/writing speed of 520/450 MB/s.

The geometric model is presented in Fig. 2 with its main details highlighted in the schematic. A tetrahedral mesh was applied to the model resulting in 1.305.219 elements, 33.088.672 degrees of freedom (DOF), and a mesh quality (skewness) of 0.68. Tetrahedral elements were applied with mesh refinement in regions of greater error, such as the weld joint, the inlet and outlet of the flow, and the internal

surface of the pipe, where the fluid interacted with the wall and the hydrodynamic boundary layer was located. Boundary-layer-type elements were used in the fluid domain in the vicinity of the wall, and in the external surfaces where the induced eddy current flowed.

## Physics and Mathematical Equations Implemented in the FEM

Welding is a multiphysics process involving several phenomena occurring simultaneously, such as conduction, convection, and radiation heat transfer, in addition to plasma jet phenomena and current flow. Solid-state phase transformations, deformation, and residual stresses are also effects occurring during welding. Creating a model that simulates and solves all of the physics simultaneously is not tractable, either due to hardware issues, computational time, or the impossibility of measuring some physical phenomena to validate the model. However, assuming some simplifications, the FEM is a powerful tool to estimate some variables and effects.

The multiphysics model in this work solved heat transfer, fluid flow, and induction heating equations. From the thermal point of view, the temperature distribution in solid domains can be described by the general tridimensional energy balance equation, given by its differential form in Equation 1, which considers the main physical properties of the material.

$$\left\{ \frac{\partial}{\partial x} \left[ k(T) \frac{\partial T}{\partial x} \right] + \frac{\partial}{\partial y} \left[ k(T) \frac{\partial T}{\partial y} \right] + \frac{\partial}{\partial z} \left[ k(T) \frac{\partial T}{\partial z} \right] \right\} + \dot{Q}(T, t) = \rho(T) C_p(T) \frac{\partial T}{\partial t} \quad (1)$$

**Table 1 – Parameters Applied to the Circumferential Weld**

Parameters of GMAW-P	
Pulse current (Ip)	380 A
Pulse time (tp)	2.7 ms
Background current (Ib)	60 A
Background time (tb)	3.5 ms
Average current (Im)	200 A
Average voltage (Um)	26.0 V
Average power (Pm)	6060 W
Wire feed speed (Wfs)	6 m/min
Contact tip to work distance (CTWD)	17 mm
Travel speed (Ts)	30 cm/min
Shielding gas	Ar + 8%CO <sub>2</sub>

where  $k$  is thermal conductivity,  $T$  is the temperature,  $\dot{Q}$  is a heat source,  $\rho$  is the density, and  $C_p$  is the specific heat.

Furthermore, the approach of this paper also considers the convective heat flux from the solid pipe wall to the fluid domain introducing an advective parcel in Equation 1. Thus, the heat transfer in the fluid domain becomes described by Equation 2, which considers the fluid physical properties and the 3-D velocity field ( $\vec{u}$ ). This velocity field is calculated by the fluid flow interface governed by Equations 3 to 10 in the turbulent regime.

$$\frac{\partial}{\partial x} \left[ k_f(T) \frac{\partial T}{\partial x} \right] + \frac{\partial}{\partial y} \left[ k_f(T) \frac{\partial T}{\partial y} \right] + \frac{\partial}{\partial z} \left[ k_f(T) \frac{\partial T}{\partial z} \right] + \dot{Q}(T, t) = \rho_f(T) C_{pf}(T) \frac{\partial T}{\partial t} + \rho_f(T) C_{pf}(T) \vec{u} \quad (2)$$

where  $k_f$  is fluid thermal conductivity,  $T$  is the fluid temperature,  $\dot{Q}$  is a heat source,  $\rho_f$  is the fluid density, and  $C_{pf}$  is the fluid heat capacity.

The equations solved in the fluid flow interface concerned the Reynolds-Averaged Navier-Stokes (RANS) model for mass and momentum conservation in turbulent regimes, described by Equations 3 and 4. In the approach, the velocity is decomposed into a 3D form according to Equation 5, while the Reynolds decomposition for turbulence is applied for each component ( $u$ ,  $v$  and  $w$ ), as exemplified in Equation 6. The turbulence model was the  $k$ - $\varepsilon$ , which considers two more transport equations, considering the turbulent kinetic energy

( $k$ ) and dissipation ( $\varepsilon$ ) according to Equations 7 and 8. Both equations consider the turbulent viscosity described in Equation 9, while the pressure is then given by Equation 10.

$$\nabla \cdot (\rho \vec{u}) = 0 \quad (\text{Mass conservation equation}) \quad (3)$$

$$\vec{u}_t + (\nabla \cdot \vec{u}) \vec{u} = -\Delta P + \frac{1}{Re} \nabla^2 \vec{u} + \rho g \quad (\text{Momentum conservation equation}) \quad (4)$$

$$\vec{u}(x, t) = \begin{bmatrix} u \\ v \\ w \end{bmatrix} = \begin{bmatrix} \bar{U} + u' \\ \bar{V} + v' \\ \bar{W} + w' \end{bmatrix} \quad (3 - D \text{ components of the velocity field}) \quad (5)$$

$$u(x, t) = \bar{U}(x) + u'(x, t) \quad (\text{Reynolds decomposition for turbulence}) \quad (6)$$

$$\rho(\nabla \cdot \vec{u})k = \nabla \cdot \left[ \left( \mu + \frac{\mu_T}{\sigma_k} \right) \nabla k \right] + P_k - \rho \varepsilon \quad (\text{Turbulent kinetic energy}) \quad (7)$$

$$\rho(\nabla \cdot \vec{u})\varepsilon = \nabla \cdot \left[ \left( \mu + \frac{\mu_T}{\sigma_\varepsilon} \right) \nabla \varepsilon \right] + C_{\varepsilon 1} \frac{\varepsilon}{k} P_k - C_{\varepsilon 2} \rho \frac{\varepsilon^2}{k} \quad (\text{Dissipation}) \quad (8)$$

$$\mu_T = \rho C_\mu \frac{k^2}{\varepsilon} \quad (\text{Turbulent viscosity}) \quad (9)$$

$$P_k = \mu_T \left[ \nabla u : (\nabla u + (\nabla u)^T) - \frac{2}{3} (u \cdot \nabla)^2 \right] - \frac{2}{3} \rho k u \cdot \nabla \quad (\text{Pressure}) \quad (10)$$

where  $Re$  is the Reynolds number,  $\rho$  is the density,  $g$  is the gravity,  $P$  is the pressure,  $\mu$  is the dynamic viscosity,  $\mu_T$  is the turbulent viscosity, and in the following constants,  $C_{\varepsilon 1} = 1.5$ ,  $C_{\varepsilon 2} = 1.9$ ,  $C_\mu = 0.09$ ,  $\sigma_k = 1.0$ , and  $\sigma_\varepsilon = 1.3$ .

The induction preheating was considered in solving the electromagnetic general theory equations in the coil group domains and in the solid pipe wall (Fig. 2). Induction heating is a function of the magnetic flux density ( $\vec{B}$ ) created by the flowing of an electric current through the coil, providing an electromagnetic driving force (voltage) induced in the part (Refs. 18, 19). To calculate the field induced by the current, it is necessary to solve Maxwell's equations (Ref. 19) in their differential forms, using a derivative approach to the magnetic vector potential ( $\vec{A}$ ) in a quasi-stationary regime ( $\nabla \times \vec{J} = 0$ ), according to the fundamental laws shown in Equation 11 to 14 and the magnetic flux density in Equation 15.

$$\nabla \times \vec{D} = \xi \text{ (Gauss' law for electric field)} \quad (11)$$

$$\nabla \times \vec{B} = 0 \text{ (Gauss' law for magnetism)} \quad (12)$$

$$\nabla \times \vec{H} = \vec{j} + \frac{\partial D}{\partial t} \text{ (Ampere's law)} \quad (13)$$

$$\nabla \times \vec{E} = -\frac{\partial \vec{B}}{\partial t} \text{ (Faraday's induction law)} \quad (14)$$

$$\vec{B} = \nabla \times \vec{A} \text{ (Magnetic flux density)} \quad (15)$$

where  $\nabla$  (del operator) is a mathematical operator that indicates the divergence of the electromagnetic field,  $\vec{D}$  is the electric flux density (C/m<sup>2</sup>),  $\xi$  is the electric charge density (C/m<sup>3</sup>),  $\vec{H}$  is the magnetic field intensity (A/m),  $\vec{E}$  is the electric field intensity (V/m),  $\vec{j}$  is the current density (A/m<sup>2</sup>), and  $E$  is the electric field intensity (V/m). To obtain a closed volume of control, in which the electromagnetic field spreads, it is necessary to couple Maxwell's equations by the constitutive relations, describing the physical properties of the medium in which the current flows. These relations are given by Equations 16 to 18.

$$\vec{B} = \mu_r \mu_0 \vec{H} \quad (16)$$

$$\vec{D} = \epsilon_r \epsilon_0 \vec{E} \quad (17)$$

$$\vec{j} = \sigma \vec{E} \quad (18)$$

where  $\mu_r$  is the relative permeability of the medium,  $\mu_0$  is the vacuum permeability (H/m),  $\epsilon_r$  is the relative permittivity of the medium,  $\epsilon_0$  is the vacuum permittivity (F/m), and  $\sigma$  is the electric conductivity of the medium (S/m).

Equations 19 to 22 describe the domain variables as the current density in the part, coil current, the current density in the coil, and the total voltage, while Equation 23 describes the magnetic insulation considered as a boundary condition to the model; that is, mathematically, there is no flux beyond the frontier of the volume of control.

$$(j\omega\xi - \omega^2\epsilon_r\epsilon_0)\vec{A} + \nabla \times (\mu_r^{-1}\mu_0^{-1}\vec{B}) = \vec{j}^e \text{ (Current density in the part)} \quad (19)$$

$$\int_{\Omega} J_i \vec{H} dS = I_{coil} \text{ (Coil current)} \quad (20)$$

$$\vec{j}^e = \frac{\xi V_i}{2\pi r} \vec{H} \text{ (Current density in the coil)} \quad (21)$$

$$V_{coil} = \sum_i V_i \text{ (Total coil voltage)} \quad (22)$$

$$n \times \vec{A} = 0 \text{ (Magnetic insulation of the volume of control)} \quad (23)$$

where  $j$  indicates an imaginary parcel,  $\omega$  is the current angular frequency,  $J_e$  is the current density,  $I_{coil}$  is the coil current,  $V_{coil}$  is the coil voltage,  $V_i$  is the voltage of a single turn of the coil, and  $n$  indicates the normal direction.

The welding heat source implemented in the model was the double ellipsoidal volumetric distribution presented by Goldak and Akhlaghi (Ref. 20). This heat distribution is divided into frontal and rear portions totalizing the entire heat source ( $qf + qr$ ). Frontal and rear portions are given by Equations 24 and 25, respectively:

$$qf(x, y, z, t) = \frac{6\sqrt{3}f_f Q}{abc_f \pi \sqrt{\pi}} \exp\left(-\frac{3x^2}{a^2}\right) \exp\left(-\frac{3y^2}{b^2}\right) \exp\left(-\frac{3[z + Ts(\tau - t)]^2}{c_f^2}\right) \quad (24)$$

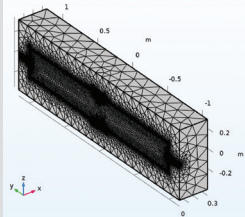
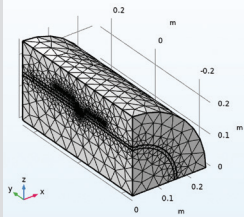
$$qr(x, y, z, t) = \frac{6\sqrt{3}f_r Q}{abc_r \pi \sqrt{\pi}} \exp\left(-\frac{3x^2}{a^2}\right) \exp\left(-\frac{3y^2}{b^2}\right) \exp\left(-\frac{3[z + Ts(\tau - t)]^2}{c_r^2}\right) \quad (25)$$

where  $f_f + f_r = 2$ ,  $Ts$  is the travel speed,  $\tau$  is a delay factor, and  $Q$  is the input power and the product of welding current ( $I$ ), voltage ( $U$ ), and thermal efficiency ( $\eta$ ).

Since the welding process was GMAW-P, the input power in the mathematical equations is presented in Table 1, and the thermal efficiency factor ( $\eta$ ) was 0.85 based on the literature (Ref. 21). The process input power ( $Q$ ) can be estimated by Equation 26, using the product of instantaneous current ( $I$ ) and voltage ( $U$ ) divided by the number measurement ( $N$ ) using the acquisition system IMC-SAP.

$$Q = \frac{\sum_{i=1}^n (U_i \times I_i)}{N} * \eta \quad (26)$$

**Table 2 – Comparison of Statistical Data Between Meshes Applied to Full-Size and Reduced Models**

	Full Size with Axial Symmetry	Reduced Size 1/4 of the Circumference
General view of geometry and mesh		
Total number of elements	1305219	187758
Skewness	0.6831	0.6563
DOF Step 1 (Nonisothermal fluid flow)	33081470	
DOF Step 2 (Electromagnetic field)	30880262	6451209
DOF Step 3 (Induction preheating)	33081470	6481282
DOF Step 4 (Welding)	33088672	6482362
Total computational time	24 h 21 min 56 s	1 h 46 min 16 s

## Results and Discussion

### Multiphysics Model for In-Service Welding Qualification

This section presents the multiphysics model to simulate in-service welding qualifications. Figure 3 shows the temperature distribution simulated in the external wall of the pipe using the induction heating equations coupled with the energy balance and fluid flow. A homogeneous temperature is verified along the pipe’s circumference according to the image. The homogeneity of the temperature distribution is an important aspect of preheating, as mentioned by Turichin et al. (Ref. 22) and Cicic et al. (Ref. 23). Conventionally applied, it is more difficult to ensure uniform heating with flame preheating compared to, for example, induction. Such uniformity of induction ensures similar preheating temperatures and similar cooling rates throughout the pipe diameter. The maximum temperature beneath the coil was 134°C (273.2°F) measured experimentally by a thermocouple in the center of the wrap, but the model indicated 115°C (239°F) at the same point, an error of 14.2%. This error might have stemmed from possible water vapor formation inside the pipe during the experimental tests, as the temperature exceeded 100°C (212°F) on the wall. Dhir (Ref. 24) demonstrated that bubble formation can occur near the wall in some cases, altering the heat transfer in the thermal boundary layer. However, in this model, the water properties have been considered nonlinear as a function of temperature (Appendix 1), but this

simulation does not model two-phase flows in the presence of bubble formation.

Regarding the temperature profile on the pipe wall (external surface), a great agreement between thermography and simulation was verified. Figure 4A presents a thermographic image of the temperature regime condition simulated in Fig. 3, while Fig. 4B shows the temperature profile on the pipe wall, as indicated by the dashed line. The thermocouples attached to the pipe wall were the reference values to the thermographic image resulting in an emissivity of 0.73 at the surface. This first simulation was used to set up and converge the induction heating running coupled with the nonisothermal flow since the complexity of the multiphysics model requires a step-by-step approach, as also used in other multiphysics models in the literature (Refs. 25–27).

Secondly, the validation of the simulation was defined by the meeting of the thermographic temperature profile and the FEM. The relatively low error in the peak temperature was acceptable considering the influence of several variables, although Kennedy et al. (Ref. 28) showed errors on the order of 1.5% in the modeling of induction heating and magnetic fields.

The in-service welding complete model developed in this research works on a sequential approach of four steps. It is possible to run each step solely to validate the results or for comparison purposes. For example, the first step’s result can be considered the fluid flow velocity field, which can be seen in Fig. 5. The streamlines presented in the image exhibit the water flowing profile inside the pipe for 380 l/min. Large vortices near the entrance were formed due to

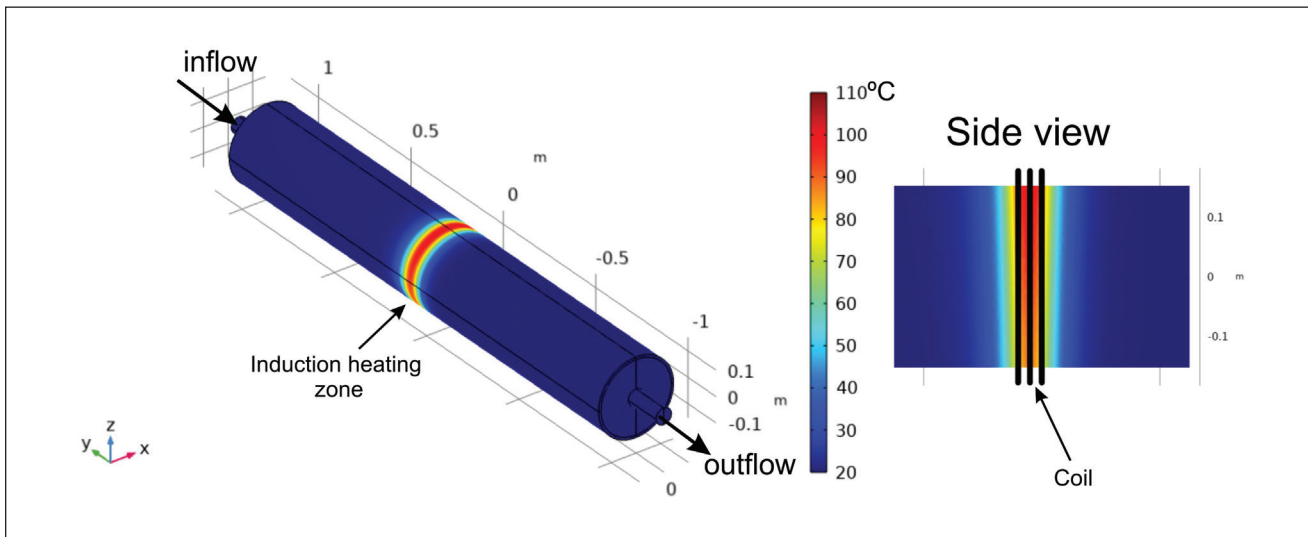


Fig. 3 – Temperature distribution in the post-processing in the pipe's external circumference.

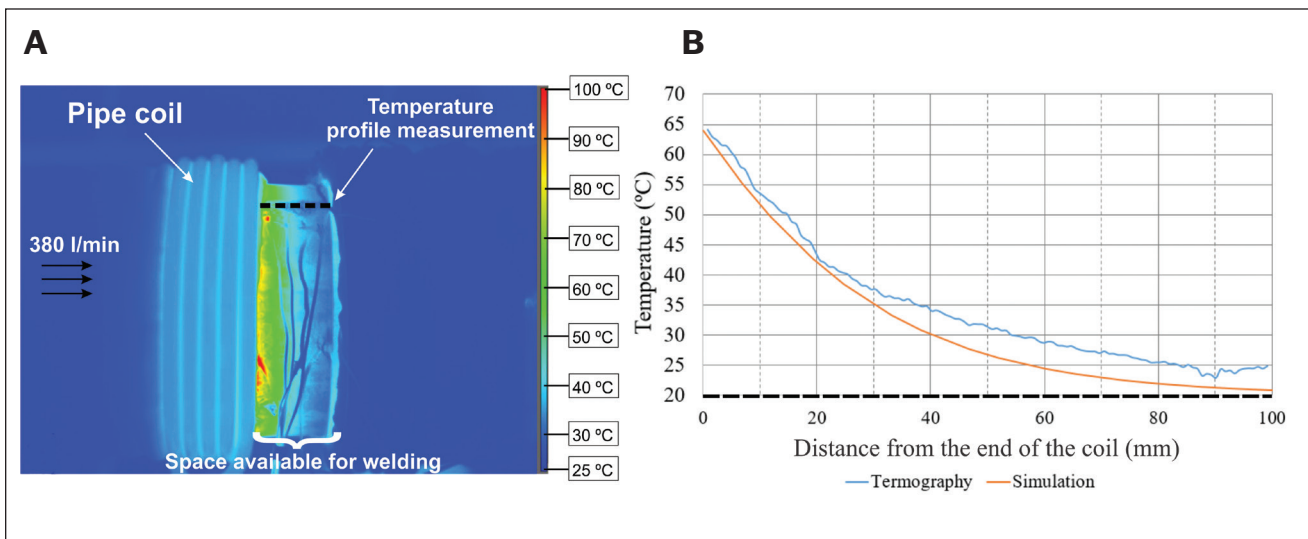


Fig. 4 – Comparison between experimental measurements (thermography) and simulation.

diameter enlargement and water recirculation at these zones. After the large vortices region (approximately half of the pipe length), the simulated streamlines indicated a more laminar flow. Fluid modeling is helpful in identifying the flow behavior in the different zones, enabling the proper setting of the position of the coil for in-service welding qualifications. Different heat transfer amounts are expected by comparing the vortices zone with the uniform region, which can affect the welding results for qualifications. Such behavior is not mentioned nor considered in the standards for in-service welding qualifications with reduced scales. Xu et al. (Ref. 29) presented the great difference between flowing with vortices characteristics versus a uniform profile by means of heat transfer characteristics. From the welding point of view, qualifying a procedure in conditions with different flow profiles can lead to mistaken conclusions due to distinct welding cooling rates and the resulting microstructure.

From the electromagnetic simulation step, the result taken from the FEM is the divergence of the magnetic field within the air domain, as shown in Fig. 6. Magnetic flux density lines (black) in the air domain indicate a stronger electric field between the coil turns and the part surface. Higher current density can be verified in the parts' wall (pipe and sleeve) beneath its surface, according to the current density colored scales. The peak current density indicated in the simulation was  $3.5 \times 10^7 \text{ A/m}^2$  on the sleeve's surface and  $1.4 \times 10^8 \text{ A/m}^2$  in the coil section. Due to the smaller cross-section area of the coil, a greater current density is expected on it. Such surface phenomenon is named the skin effect, also cited by Ocilka and Kovác (Ref. 18), in which most of the current circulates throughout a thin layer of the part, creating heating by the Joule effect. Li et al. (Ref. 15) mentioned that due to the internal heat generation provided by the skin effect, lower

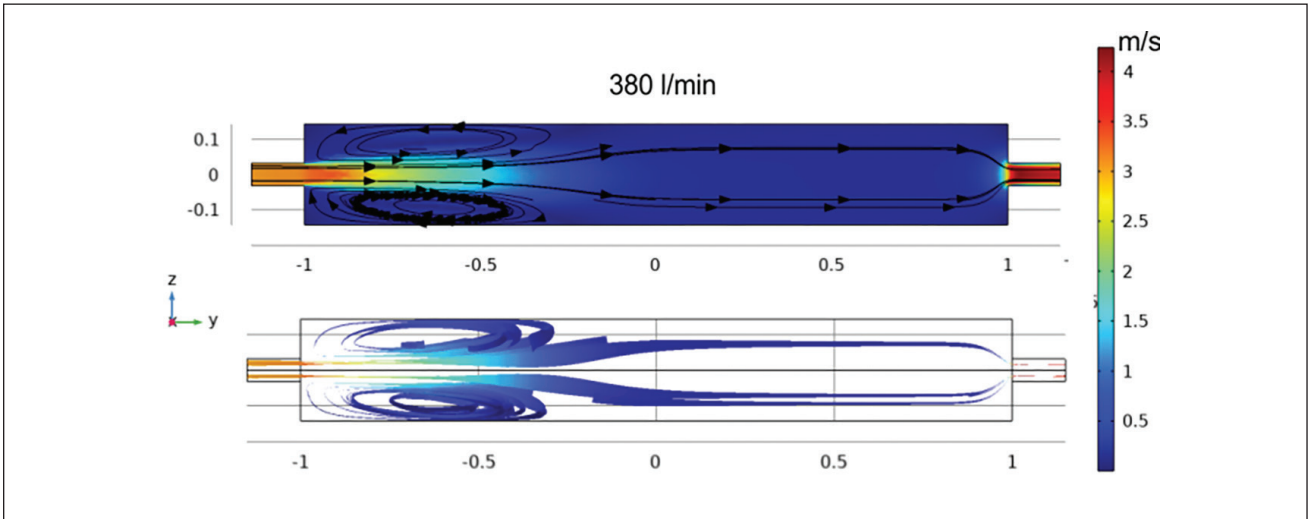


Fig. 5 – Velocity gradient and streamlines of the fluid flow inside the pipe for 380 l/min.

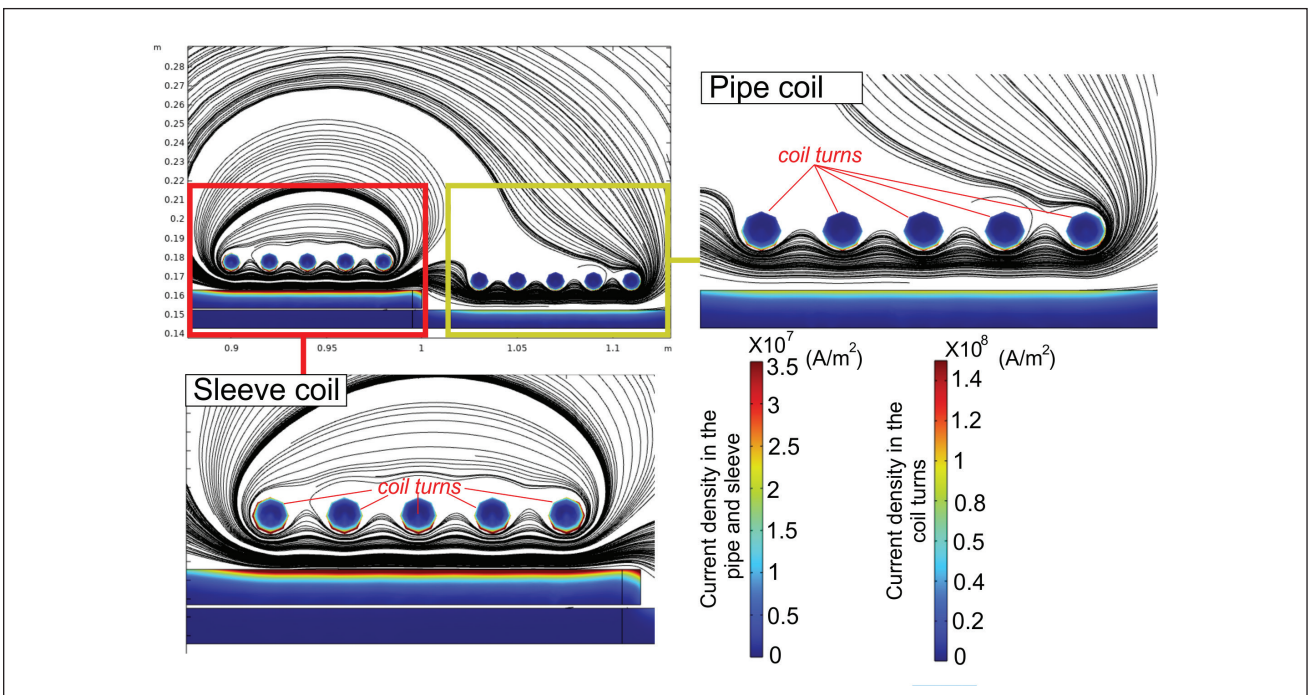


Fig. 6 – Electromagnetic flux density lines and current density in the part and in the coil.

heat losses are expected, and greater efficiency is obtained in induction heating.

Step 3 of the model calculates the preheating based on the calculated electromagnetic field from Fig. 6. Thus, Step 2 generates a heat source that is an input parameter of Step 3, in which the heat transfer balance equation is accounted for. Figure 7 shows the transient analysis of the temperature using the two coils from Step 2. To control the preheating level, a Boolean logic (on/off) was programmed in the software to control the coil current and simulate the experimental behavior of the induction power source. Thus, the maximum temperature of 400°C (752°F) was hit in 15 s and controlled at that value afterward. Due to the fluid flow and forced con-

vection, the temperature was lower in the pipe's wall for the same power applied to the sleeve. For instance, after 20 s (thermal regime condition), the highest temperature in the pipe was 115°C (239°F) beneath the coil and 90°C (194°F) in the joint location.

Finally, Step 4 solved the temperature transient analysis by implementing the welding heat source with the double ellipsoidal distribution. Figure 8 shows the temperature distribution for 5 s, 10 s, and 20 s beside a colored cross-section scale of the fluid velocity. The last calculated time step of the induction preheating from Fig. 7 provided the initial temperature and fluid velocity of the welding step. Thus, in that case, the maximum temperature started from 400°C in

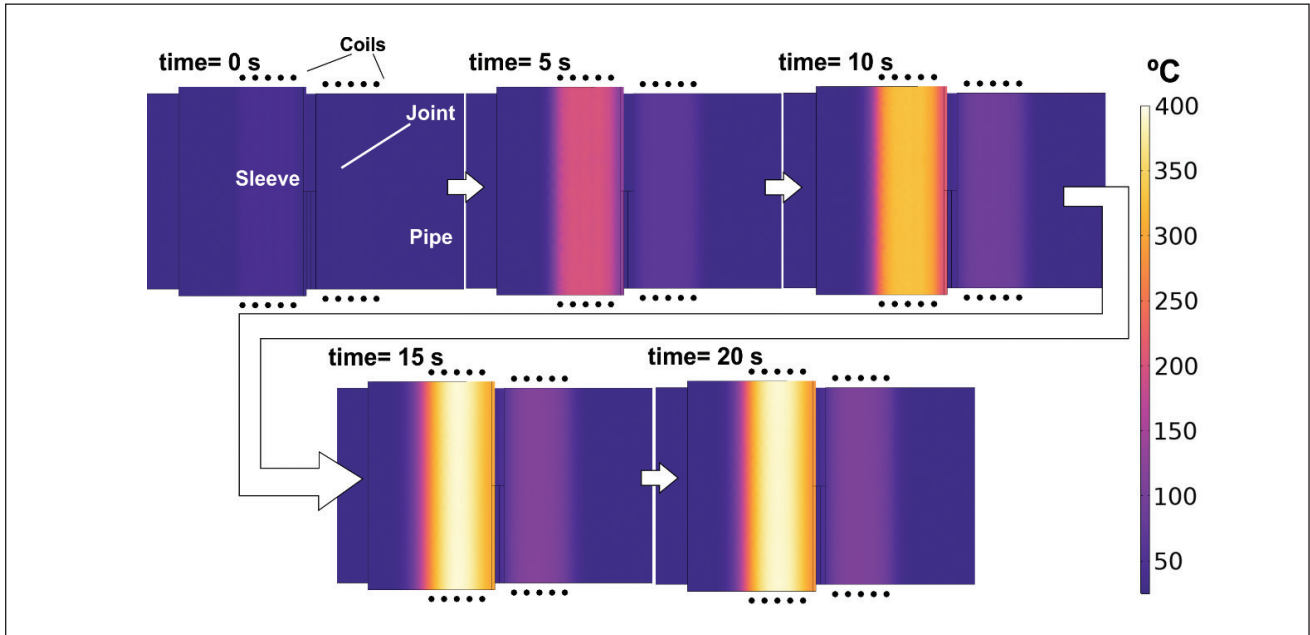


Fig. 7 – Transient analysis of the preheating temperature in the sleeve and pipe.

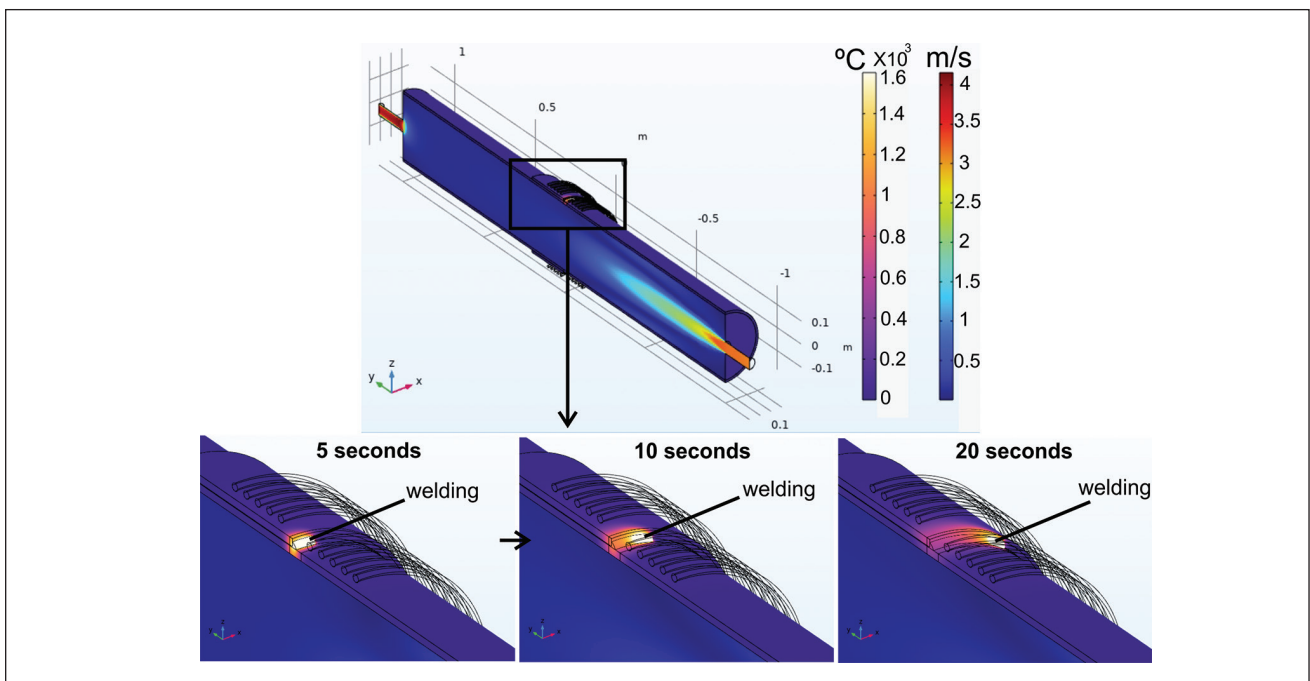


Fig. 8 – Fully coupled multiphysics model of an in-service welding qualification.

the sleeve and 90°C in the pipe. Such logical programming was set in the software using its own configuration interface by adopting the initial values of Step 4 as the last calculated time step from Step 3.

The mesh developed for a multiphysics model must also consider the peculiarity and features suitable for each physic. Solving electromagnetic heating requires finer elements near the surface where the eddy current flows. Most of the in-service welding simulations available in the literature neglect

solving the fluid flow and do not consider pre-heating power source distribution (Refs. 11–14). Generally, only the welding analysis is simulated using a constant value of the  $h$  coefficient for the entire internal surface, although the literature points out the significant difference in the consideration of local heat transfer versus an overall coefficient (Refs. 30, 31).

Time consumption is also an important factor to be considered when solving a large multiphysics model (Refs. 9–11, 12). The complete welding model in Fig. 8 (fluid flow + induction

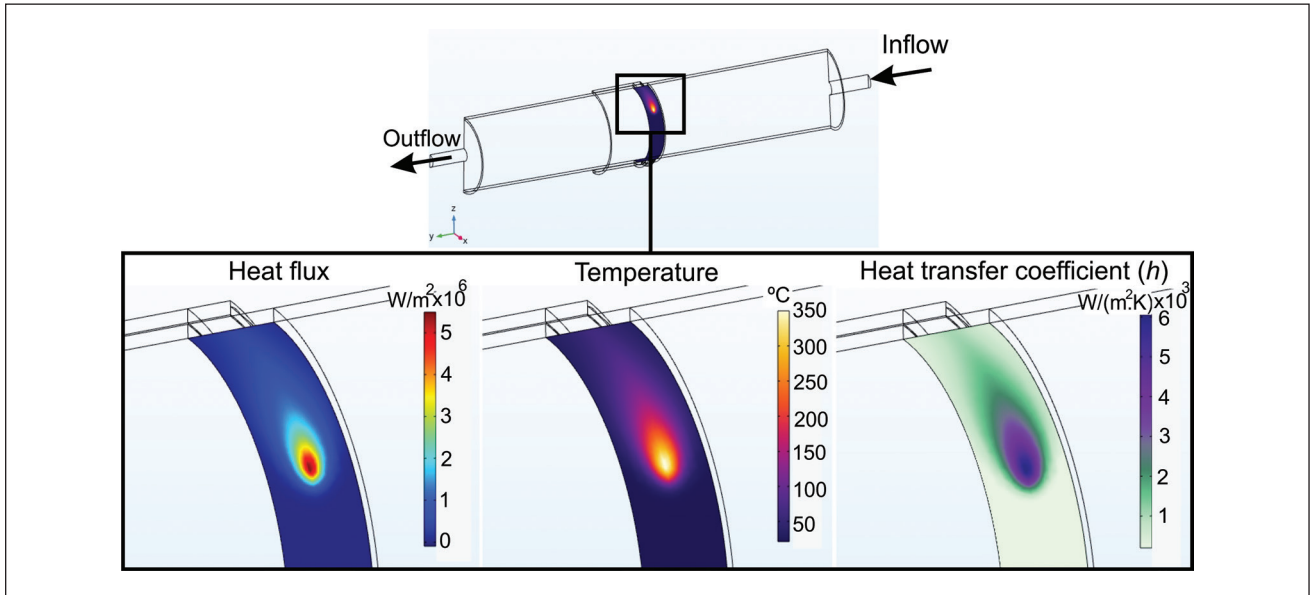


Fig. 9 – View of the inner surface showing in the post-processing, the plot of heat flux ( $W/m^2$ ), temperature ( $^{\circ}C$ ), and heat transfer coefficient ( $W/(m^2K)$ ).

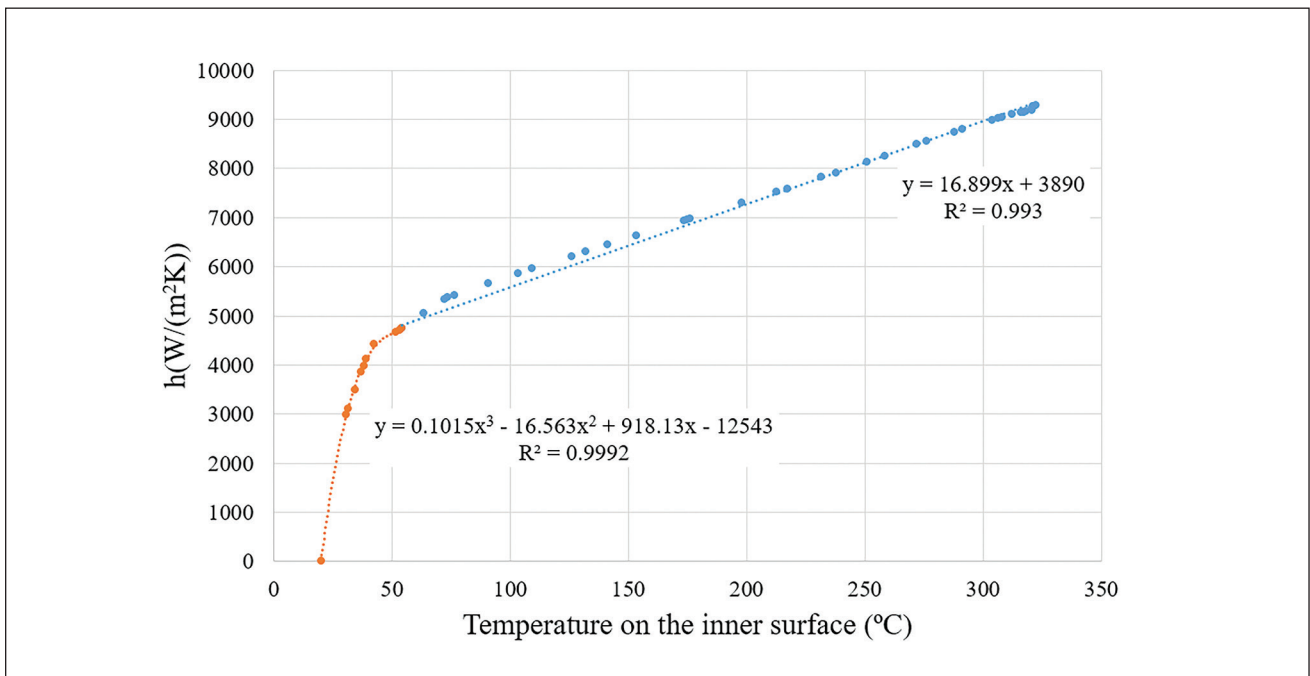


Fig. 10 – Correlation between the heat transfer coefficient and the temperature at the inner wall.

+ welding) took approximately 24 h of calculation to finish all four steps. Discretizing the simulation into paces enables solving a problem with many DOFs since each physic can be solved independently in its respective step and further mathematically coupled using the initial values of the previously calculated variables as boundary conditions, facilitating the convergence. Such a method avoids the necessity of the computer mounting the entire problem at the same time with all DOFs, and dividing the solution into steps makes

the convergence of the subsequent steps faster since the initial values are input from the already converged previous solution. An example of this case is fluid flow, which is first simulated in Step 1 up to its flow regime condition (Fig. 5), and the last calculated time step feeds the initial time of steps 3 and 4, keeping the flowing water while induction preheating and welding are calculated.

However, time consumption makes the applicability of the model questionable for quick tests. Thus, to reduce time

processing, an approach to enter directly with the convection coefficient was used based on the full-scale model previously calculated. The  $h$  coefficient was input in the model as a boundary condition. This approach enabled work with reduced geometry and eliminated the necessity of considering the fluid flow for every single step since the heat transfer was considered variable locally depending on heat flux and temperature on the inner surface. The  $h$  coefficient can be calculated in the post-processing of the multiphysics model of Fig. 8, according to Equation 27.

$$h = \frac{-k \frac{dT}{dn}}{(T_w - T_\infty)} \quad (27)$$

where  $k$  is the thermal conductivity,  $dT/dn$  is the normal temperature gradient across the pipe wall,  $T_w$  is the wall temperature, and  $T_\infty$  is the fluid temperature. Therefore,  $h$  is variable locally depending on heat flux, wall temperature, and fluid properties. Such local variation of  $h$  can be seen in the correlation with temperature in Fig. 9, in which the higher the heat flux through the wall, the higher the heat transfer coefficient. Fig. 9 presents an internal view of the pipe's wall with the moving welding heat source applied on the external side. It is possible to verify that the peak value of the  $h$  coefficient moved with the welding heat source due to the greater heat flux at its center. The peak temperature on the internal wall was about 350°C (662°F), which is also an important index for in-service welding, and it is way down from the maximum temperature of 980°C (1796°F) considered in the literature for most in-service applications (Refs. 1, 2).

Figure 10 shows the correlation between temperature and convection coefficient on the internal surface. The value of  $h$  as a function of temperature was captured in the results post-processing and transformed into a temperature-dependent variable, according to the system of Equation 28. From Equation 28 it can be seen that at  $T_{wall} = 20^\circ\text{C}$  (68°F) (at the same temperature as the fluid), there was no heat flux and  $h$  was 0. When wall temperature increased due to the welding, the  $h$  coefficient increased.

Different from general approaches in the literature presented by Huang et al. (Ref. 11) and Alian et al. (Ref. 13), the value of  $h$  was considered based on a simulation of the real fluid flow obtained numerically instead of equations for fully developed flows, which are not applicable in reduced-length samples commonly applied for in-service welding qualifications. Moreover, the employment of equations for fully developed flows can lead the FEA to great errors in temperature distribution and welding thermal cycles comparing the simulated data with experiments.

$$h(T_{wall}) = \begin{cases} 0, & \text{if } T_{wall} = 20^\circ\text{C} \\ 0.10157T^3 - 16.563T^2 + 918.13T - 12543, & \text{if } 20^\circ\text{C} < T_{wall} \leq 55^\circ\text{C} \\ 16.8997T + 3890, & \text{if } 55^\circ\text{C} < T_{wall} \end{cases} \quad (28)$$

Getting the change of  $h$  as a function of the temperature enables working with reduced geometries in the in-service welding simulation once the fluid flow parameters and the mock-up's geometry and dimensions are kept the same during a qualification procedure. Therefore, it is possible to use Equation 28 as a boundary condition on the inner surface while setting the heat transfer physic. The model was then reduced to represent only a quarter of the pipe circumference with a reduced length of 500 mm (19.685 in.), assuming that regions too far from the welding can be negligible in terms of heat flux. Table 2 compares the statistical data of the full-scale model with the reduced-scale one. Reducing the geometry significantly shortened the number of DOFs and the total computational time. The time was reduced to 1 h, 46 min for a complete FEA of the temperature distribution and the thermal cycles simulation.

Consequently, in Part 2 of this work, a comparison between the simulated molten zone area, temperature distribution, and thermal cycles will be presented and discussed in order to validate the model presented in Part 1. A method to estimate the microstructure using continuous cooling transforming curves and the experimental evaluation of the microstructure using microscopy will also be discussed.

## Conclusions

The present work showed a multiphysics model to simulate in-service welding qualifications focused mainly on thermal analysis. Part 1 proposed solving Maxwell's equations, mass conservation, Navier-Stokes, and heat transfer balance in a coupled approach. Thus, the following conclusions can be stated:

- Simulating the fluid flow and preheating source differs from the usual literature for in-service welding simulations and enables us to study specific cases in comparison with real repairs.
- An error of 14.2% was obtained comparing the peak temperature of induction preheating simulation and experimental data. Further research will address modeling considerations for possible two-phase fluid flow to minimize the error.
- The multiphysic model greatly approximated the temperature distribution on the pipe's wall for induction preheating.
- The simulated streamlines showed different flow zones in reduced-length mock-ups for in-service welding qualification, which may result in different cooling rates along the pipe.
- The electromagnetic field lines in the simulation indicated a higher current density on the surface of the pipe and the sleeve, suggesting the presence of the skin effect in the component.
- Applying the same current to the coil resulted in different heating temperatures comparing the sleeve and the pipe. Forced convection acted on the pipe wall, in which the peak temperature was 115°C, while the sleeve's temperature was controlled at 400°C. This occurred because the sleeve was partially isolated from the pipe by the gap between the parts.
- Solving a complex multiphysics model can make the simulation not applicable for quick tests. Entering the local  $h$  on the inner pipe's surface as a function of temperature,

based on a full-scale simulation, is an alternative since the processing time was reduced from 24 h to 1 h, 46 min. The lower time was achieved by reducing the model size to ¼ of the pipe diameter and the number of elements from 1305219 to 187758.

■ Working with coupled multiphysics makes way for the implementation and FEA of the effect of simultaneous variables on the in-service welding application. Future publications will explore the mechanical behavior of the welded joint, considering residual stress and deformation.

## Acknowledgments

The authors would like to acknowledge the LABSOLDA staff for technical support throughout the time in which this work was developed, as well as the researchers from OSU/EJTC for the technical advisement in some important steps. In the same way, the authors appreciate the funding support of Petrobras, POSMEC, and the CNPQ.

## References

1. Bruce, W. A. 2002. Qualification of procedures for welding onto in-service pipelines. *Proceedings of the 4th International Pipeline Conference*, 39-53. Calgary, Alberta, Canada. DOI: 10.1115/IPC2002-27131
2. Bruce, W. A., Holdren, R. L., Mohr, W. C., and Kiefner, J. F. 1996. Repair of pipelines by direct deposition of weld metal further studies. *Final Report*. United States.
3. Tronskar, J. P., Tornqvist, R., Guan, O. H., and Bruce, W. A. 2015. "Live" repair of gas pipeline with deep girth weld crack. *Proceedings of the ASME 2015 Pressure Vessel and Piping Conference*. Boston, Mass.: ASME. DOI: 10.1115/PVP2015-46005
4. Batisse, R., and Hertz-Clemens, S. 2008. A review of various repair techniques for gas transmission pipelines: advantages, limitations and developments. *Gfd Suez France. International Gas Union Research Conference*. Paris, France. DOI: 10.1007/978-1-4020-6526-2\_20
5. Farzadi, A. 2016. Gas pipeline failure caused by in-service welding. *Journal of Pressure Vessel Technology*, 138(1): 011405. DOI: 10.1115/1.4031443
6. API Standard 1104. 2007. *Standard for welding pipelines and related facilities*. American Petroleum Institute, USA. 50.
7. Jaske, C. E., Hart, B. O., and Bruce, W. A. 2006. *Pipeline repair manual – 6th Edition*. Pipeline Research Council International (PRCI). Arlington, Virginia.
8. Bruce, W. A., and Bradley, C. E. 2012. Further development of heat-affected zone hardness limits for in-service welding. *Proceedings of the 2012 9th International Pipeline Conference*. Calgary, Alberta, Canada. DOI: 10.1115/IPC2012-90095
9. Sabapathy, P. N., Wahab, M. A., and Painter, M. J. 2000. The prediction of burn-through during in-service welding of gas pipelines. *International Journal of Pressure Vessels and Piping* 77: 669–677. DOI: 10.1016/S0308-0161(00)00056-9
10. Boring, M. A., and Bruce, W. A. 2008. The effect of hoop stress on the burnthrough susceptibility during in-service welding of thin-walled pipelines. *Proceedings of the 7th International Pipeline Conference*. Calgary, Alberta, Canada. DOI: 10.1115/IPC2008-64354
11. Huang, Z., Tanga, H., Dingb, Y., Weic, O., and Xiac, G. 2017. Numerical simulations of temperature for the in-service welding of gas pipeline. *Journal of Materials Processing Technology* 248: 72–78. DOI: 10.1016/j.jmatprotec.2017.05.008
12. Guest, S., Dyck, J., Egbewande, A., MacKenzie, R., and Sadowski, M. Design of in-service repair welding procedures for operating pipelines: critical assessment of variables affecting restraint level and heat-affected zone microstructures of vintage pipelines. *Proceedings of the 2016 11th International Pipeline Conference*. Calgary, Alberta, Canada. DOI: 10.1115/IPC2016-64206.
13. Alian, A. R., Shazly, M., and Megahed, M. M. 2016. 3D Finite element modeling of in-service sleeve repair welding of gas pipelines. *International Journal of Pressure Vessels and Piping* 146: 216–229. DOI: 10.1016/j.ijpvp.2016.09.002
14. Wang, Y., Wang, L., Di, X., Shi, Y., Bao, X., and Gao, X. 2013. Simulation and analysis of temperature field for in-service multi-pass welding of a sleeve fillet weld. *Computational Materials Science* 68: 198–205. DOI: 10.1016/j.commatsci.2012.10.025
15. Li, L., Mi, G., and Wang, C. A. 2019. A comparison between induction pre-heating and induction post-heating at laser-induction hybrid welding an S690QL steel. *Journal of Manufacturing Processes* 43: 276–291. DOI: 10.1016/j.jmapro.2019.05.003
16. Ikram, A., Arif, N., and Chung, H. 2016. Design of an induction system for induction assisted alternating current gas metal arc welding. *Journal of Materials Processing Technology* 231: 162–170. DOI: 10.1016/j.jmatprotec.2015.12.015
17. IMC Welding. Portable Acquisition System. Available on: <https://www.imc-soldagem.com.br/pt-br/equipamentos/sistemas-de-monitoramento/sap-v4ti>.
18. Ocilka, M., and Kováč, D. 2015. Simulation model of induction heating in COMSOL Multiphysics. *Acta Electrotechnica et Informatica* 15(1): 29–33. DOI: 10.15546/aei-2015-0005
19. Fitzpatrick, R. 2008. *Maxwell's Equations and Principles of Electromagnetism*. Burlington: Jones & Bartlett Learning.
20. Goldak, J. A., and Akhlaghi, M. 2005. *Computational Welding Mechanics*. DOI: 10.1007/b101137
21. Joseph, A., Harwig, D., Farson, D. F., and Richardson, R. 2003. Measurement and calculation of arc power and heat transfer efficiency in pulsed gas metal arc welding. *Science and Technology of Welding and Joining* 8(6). DOI: 10.1179/136217103225005642
22. Turichin, G., Kuznetsova, M., Pozdnyakov, A., Gook, S., Gumenyuk, A., and Rethmeier, M. 2018. Influence of heat input and preheating on the cooling rate, microstructure and mechanical properties at the hybrid laser-arc welding of api 5l x80 steel. *Proceedings of the 10th CIRP Conference on Photonic Technologies* 748–751. DOI: 10.1016/j.procir.2018.08.018
23. Cacic, D. T., Rontescu, C., Bogatu, A. M., and Petriceanu, C. S. 2018. Research regarding the influence of the preheating temperature on the welding dilution. *IOP Conference Series: Materials Science and Engineering* 400:2. DOI: 10.1088/1757-899X/400/2/022015
24. Dhir, V. K. 1998. Boiling heat transfer. *Annual Review of Fluid Mechanics* 30: 365–401. DOI:10.1146/annurev.fluid.30.1.365
25. Kong, F., and Humrickhouse, P. W. 2022. Toward a fully integrated multiphysics simulations framework for fusion blanket design. *IEEE Transactions on Plasma Science* 50(11). DOI: 10.1109/TPS.2022.3173158
26. Guan, S., He, X., Wang, X., and Hua, L. 2020. Multiphysics simulation of the resistance spot welding detection using electromagnetic ultrasonic transverse wave. *The International Journal of Advanced Manufacturing Technology* 110: 79–88. DOI: 10.1007/s00170-020-05809-6
27. Pawar, S., and Sharma, A. 2019. Multiphysics simulation of welding-arc and nozzle-arc system: mathematical-model, solution-methodology and validation. *Journal of The Institution of Engineers India Series C* 100: 145–152. DOI: 10.1007/s40032-017-0430-6
28. Kennedy, M. W., Akhtar, S., Bakken, J. A., and Aune, R. E. 2011. Analytical and experimental validation of electromagnetic simulations using COMSOL®, re inductance, induction heating and magnetic

fields. *Proceedings of the 2011 COMSOL Users Conference*, Stuttgart, Germany.

29. Xu, Z., Han, Z., Wang, J., and Liu, Z. 2018. The characteristics of the heat transfer and flow resistance in a rectangular channel with vortex generators. *International Journal of Heat and Mass Transfer* 116: 61–72. DOI: 10.1016/j.ijheatmasstransfer.2017.08.083

30. Bai, B., He, Y., Li, X., Hu, S., Huang, X., Li, J., and Zhu, J. 2016. Local heat transfer characteristics of water flowing through a single fracture within a cylindrical granite specimen. *Environment Earth Sciences* 75: 1640. DOI: 10.1007/s12665-016-6249-2

31. Liu, S., Mu, X., Shen, S., Li, C., and Wang, B. 2021. Experimental study on the distribution of local heat transfer coefficient of falling film heat transfer outside horizontal tube. *International Journal of Heat and Mass Transfer* 170: 121031. DOI: 10.1016/j.ijheatmasstransfer.2021.121031

## Appendix 1

### Model Boundary Conditions

This appendix shows the boundary conditions and the materials' physical properties considered in each of the physics solved in the model described in the paper.

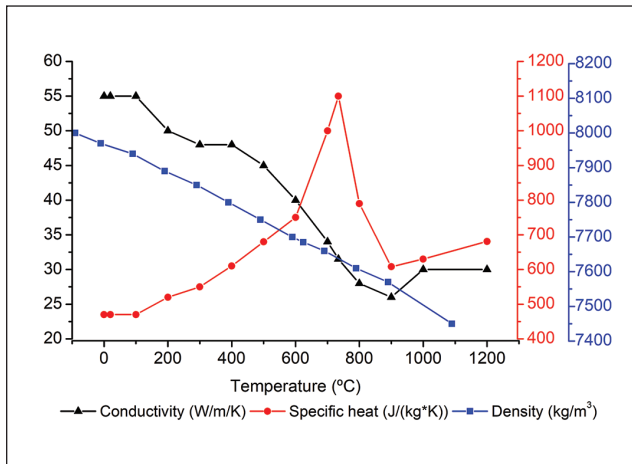


Fig. A1 – Carbon steel's physical properties.

## Heat Transfer in Solids and Fluids

In the thermal analysis, the boundary conditions considered were the room temperature at 25°C (77°F) and convection heat transfer to the environment applying the correlation presented by Incropera et al. (Ref. 1) for horizontal cylinders. The pipe domain was set as carbon steel and the nonisothermal flow with the water properties. The carbon steel's physical properties are presented in Fig. A1, while the water properties are presented in Fig. A2.

### Fluid Flow (Turbulent Flow)

In turbulent fluid flow physics, Equations 3–10 presented in the manuscript were solved. Due to the coupling between heat transfer and fluid flow, the water properties from Fig. A2 were also input conditions in this step. The flow was also set as weakly compressible with density evaluated at the reference pressure and considering its function with temperature (temperature-dependent). The inlet and outlet flow faces were defined according to Fig. A3, and the gravity force was considered constant (9.81 m [32.254 ft]/s<sup>2</sup>) acting in the z-axis direction.

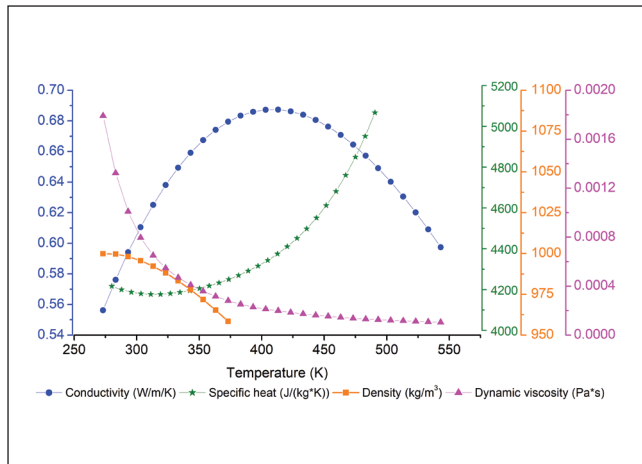


Fig. A2 – Water's physical properties.

Table A1 – Magnetic and Electric Properties Applied to the Simulation

Properties	Air	Copper	Carbon Steel
Electric conductivity (S/m)	$1 \times 10^{-12}$	$5.998 \times 10^7$	$4.032 \times 10^6$
Relative permeability		1	
Relative permittivity		1	
Vacuum permeability (H/m)		$4\pi \times 10^{-7}$	
Vacuum permittivity (F/m)		$8.85 \times 10^{-12}$	

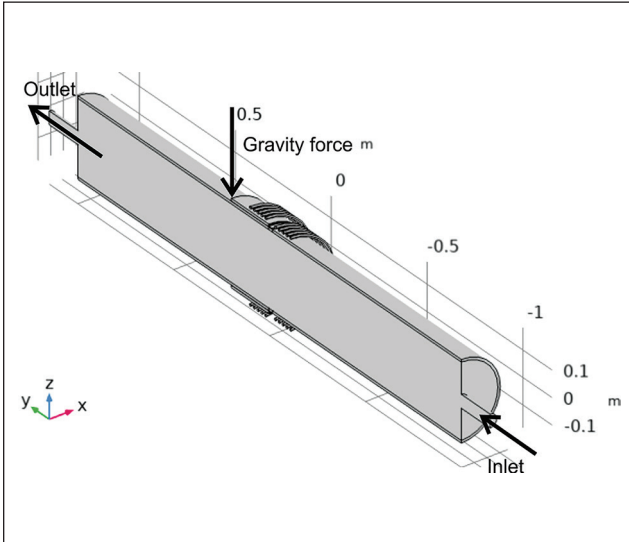


Fig. A3 – Pipe domain with the inlet and outlet boundary conditions in the fluid flow physics.

The net flow into the domain was set as a mass flow rate ( $m$ ) value, which is assumed to be parallel to the boundary surface (inlet) and tangential to the flow velocity. The  $m$  can be calculated by Equation A1 using the volume flow ( $V$ ), which was 380 l/min in this work. Due to the cooler used in the water loop, the inlet water temperature was set to constant at 20°C (68°F).

$$m = \frac{V}{2} * \rho_{water} \quad (A1)$$

where  $m$  is the mass flow rate (kg/s),  $V$  is the volume flow ( $m^3/s$ ) and  $\rho_{water}$  is the water density ( $kg/m^3$ ) at inlet temperature. As the velocity was indirectly set in the inlet, the reference pressure was set in the outlet as 1 atm.

## Magnetic Fields

In this physic, the magnetic field created due to the alternated current flow through the coil groups was calculated. According to the description in the main manuscript, it solved Maxwell's equations coupled with the heat transfer physics to account for the induction preheating provided in the pipe wall. Thus, one of the input power sources ( $\dot{Q}$ ) in the heat transfer equation (Equation 1) consisted of the power generated from the current flow and the coil voltage in the magnetic field step. As highlighted in blue in Fig. A4, magnetic induction was solved in the air box domain, pipe and sleeve walls, and in the copper coils, excluding the water domain. Thus, the electrical and magnetic properties of these materials were

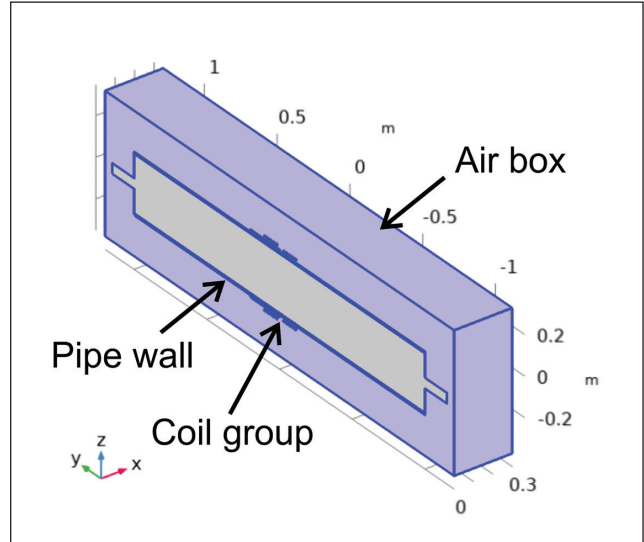


Fig. A4 – Domains selected to solve magnetic field physics.

set according to Table A1. The properties were assumed as constant for all materials with the values available on COM-SOL's database.

Coil excitation was set by an applied alternate current with an RMS current of 350 A and a frequency of 10.4 kHz. This boundary condition was defined for both coils: the one around the pipe and the second around the sleeve. These values were defined based on the electric signals' measurement of the induction power source used in the experiments (Miller ProHeat 35), as explained in the main text.

## Appendix References

1. Incropera, F. P., Dewitt, D. P., Bergman, T., and Lavine, A. 2014. *Fundamentals of Heat and Mass Transfer*, Seventh Edition. Hoboken: John Wiley & Sons.

**KAUE CORREA RIFFEL** ([riffel.12@osu.edu](mailto:riffel.12@osu.edu)) and **REGIS HENRIQUE GONÇALVES E SILVA** are with the Federal University of Santa Catarina, Florianopolis, Santa Catarina, Brazil. **ANTONIO JOSE RAMIREZ** and **ANDRES FABRICIO FISCHDICK ACUNA** are with The Ohio State University, Columbus, Ohio. **GIOVANI DALPIAZ** and **MARCELO TORRES PIZA PAES** are with Petrobras/CENPES, Rio de Janeiro, Brazil.